www.czasopisma.pan.pl   PAN   www.journals.pan.pl
POLSKA AKADEMIA NAUK

Arch. Metall. Mater. **64** (2019), 4, 1645-1652

YOSHITSUGU HANADA*, YANG XIAO*, AKIO SONODA*, HYO-GYOUNG KANG*,
HIDEAKI NAGAYOSHI*, ATSUO YAMAMOTO*, TATSUYA TOKUNAGA**

SILICON CARBIDE FABRICATION BY INFILTRATION OF MOLTEN FE-SI ALLOY
THROUGH TWO-STEP REACTION SINTERING

Wider application of silicon carbide (SiC) is anticipated for increasing the durability of various structural facilities. For this study, SiC was fabricated with decreased electrical resistivity for precision electrical discharge machining. Two-step reaction sintering by infiltration of molten Fe-Si alloy was applied for SiC fabrication. The procedure included first sintering at 973 K in Ar gas atmosphere and second sintering by spontaneous infiltration of molten Fe-75%Si alloy at 1693 K in vacuum. The sintered structure porosity became very low, forming 3C-type SiC. Results confirmed that molten Fe-75%Si alloy infiltration occurred because of reaction sintering. The electrical resistivity of the sintered SiC infiltrated by molten Fe-75%Si alloy can be improved to be two orders of magnitude lower than that by molten Si, consequently maintaining the high performance of SiC.

Keywords: electrical resistivity, fracture toughness, iron silicide, molten metal infiltration, silicon carbide

1. Introduction

Silicon carbide (SiC) is widely used as a material with excellent properties at high temperatures. Its properties include low density, high hardness, high wear resistance, high corrosion resistance, high thermal conductivity, and structural stability [1]. For future applications, SiC can be supplied stably for products. For those applications, it can provide equipment that can offer stable and secure operations over long periods because SiC heat resistance is higher than that of conventional wear-resistant materials such as iron-based alloys and compounds [2]. In addition, SiC is comprises silicon (Si) and carbon (C): materials that are unlikely to be exhausted for a long time in the Earth's crust. By contrast, conventional wear-resistant materials generally use large amounts of rare-earth metals for high performance. Substituting SiC for such materials can contribute to the conservation of rare-earth metals.

Nevertheless, SiC ceramics are too hard and brittle to machine. That shortcoming hinders their application as wear-resistant products. Resolving this shortcoming is necessary to decrease machining costs of SiC ceramics for precision parts. Furthermore, SiC ceramics cannot be machined easily in commercially available machines without expensive and specialized tools. Such difficulties lead to high costs of machining. Improving the unique characteristics of SiC dramatically is difficult to achieve merely by optimization of production methods. Resolving the difficulties described above can be accomplished by fabrication of a composite material with the desired characteristics [3]. Many researchers have studied the fabrication of SiC composites using materials such as fibers and yarns of SiC or C with an included Si matrix, and infiltration of cast iron or Al into a SiC preformed body [4-7]. The emphasis of these earlier studies is SiC reinforcement, but less research has been done to investigate the improvement of SiC machinability. A possible SiC composite production method might be reaction sintering [1,8,9]. The fabrication method includes processing by reaction of SiC and filling up of molten metal, followed by subsequent spontaneous infiltration into a porous preformed body. As a result, a composite of formed SiC and infiltrated metal is obtainable [10,11]. Generally, Si is used as an infiltration metal of reaction sintering. Various SiC composites are producible by selecting an alloy having better characteristics than those of Si [12].

For this study, we aimed at new applications of SiC ceramics for various industrial plants and tried to improve machinability of SiC ceramics. Specifically, precision electrical discharge machining is applicable for SiC ceramics [13]. Therefore, we proposed that Fe-75%Si alloy be used as the infiltration material of reaction sintering because the iron alloy has lower electrical resistivity and higher fracture toughness than those of Si [14,15]. The wettability of molten Fe-Si based alloy with a SiC substrate is reportedly as good as that of molten Si. Moreover, the alloy can be infiltrated spontaneously into the porous preformed body [16,17]. To reduce the dimensional change of the product, we also applied two-step reaction sintering: a near-net shaping process. The method

*   FUJICO CO., LTD., KITAKYUSHU, JAPAN
** KYUSHU INSTITUTE OF TECHNOLOGY, FACULTY OF ENGINEERING, KITAKYUSHU, JAPAN

Corresponding author: y-hanada.fujico@kfjc.co.jp

is regarded as effective for lowering SiC ceramics machining costs. Few reports have described SiC fabrication by infiltration of molten Fe-Si alloy through two-step reaction sintering.

This report describes introduction of the SiC fabrication method by infiltration of molten Fe-Si alloy through two-step reaction sintering. The microstructural characteristics of sintered SiC were investigated, along with its hardness, fracture toughness, bending strength and electrical resistivity of sintered SiC were investigated. Furthermore, the machinability of the sintered SiC ceramics was confirmed using electrical discharge machining.

2. Experiment and procedures

2.1. Sintering method

As starting materials, SiC powder (94 mass% pure, under 10 µm or smaller particle size), Si powder (99.99 mass%, under 5 µm or smaller particles), and C powder (99 mass%, average 47 nm particle size) were used. Phenol resin powder was used to bind the powders. The infiltration materials were Si and Fe-75 mass%Si alloy lumps of about 20 mm. As an inoculation agent for casting, Fe-75 mass%Si alloy is commonly used. Three combinations of specimens with changed composition and infiltration metal were prepared for experiments, as shown in Table 1. These samples were labeled as SiC-1, SiC-2, and SiC-3. A powder blend of SiC, Si, and C and resin at a weight ratio of SiC : Si : C : resin = 73 : 2 : 9 :16 was selected for a preparation experiment to assess the easy infiltration condition of molten Fe-Si alloy. The raw material powders were weighed, dried, and mixed for 86.4 ks using a rotary agitator with a mill vessel and zirconium balls.

TABLE 1

Compositions of sintering samples

Sample	Raw material	Sintering material
		mass%
SiC-1	73%SiC-2%Si-9%C-16%Resin	100%Si
SiC-2		Fe-75%Si
SiC-3	42%Si-42%C-16%Resin	

Fig. 1 presents a fabrication process flowchart. The procedures were of forming, first-sintering, second-sintering, and cooling. First, during step forming, dried and mixed powders were hot-pressed at 473 K under axial pressure of 20 MPa. The mold size was 50 × 50 × 20 mm. After cooling, the formed body was removed from the mold. Next, in the step of first sintering, a porous preformed body was sintered by heating at 973 K for 3.6 ks in Ar gas atmosphere furnace. Then, during second-sintering, the molten metal was infiltrated into the sintered body by heating at 1693 K for 900 s in vacuum (below 10 Pa). Before furnace heating, the preformed body was put into a dense graphite crucible. The infiltration metal was then added to cover the preformed body. During furnace heating, the preformed body was immersed entirely in the molten metal in the crucible. Finally, the sintered body was cooled to room temperature, which took 36 ks.
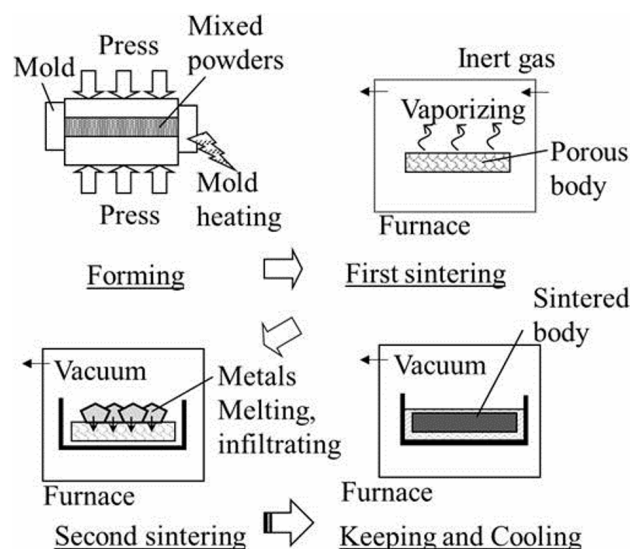

Fig. 1. Flowchart of fabrication process by two-step reaction sintering of SiC

A schematic illustration of two-step reaction sintering for SiC is presented in Fig. 2. During first-sintering, part of the resin component was vaporized from the body. The resin was carbonized to a C component: SiC was formed simultaneously by reaction of the Si and C in the body. During second-sintering, SiC was formed by reacting the Si component of the infiltrated alloy and the C component of the preformed body.
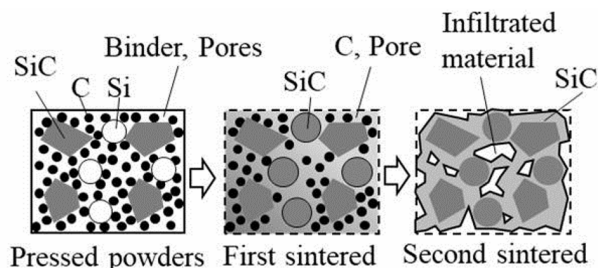

Fig. 2. Schematic illustration of the two-step reaction sintering method

2.2. Measurement method

Before any measurement, the sintered body surfaces were mirror-polished using a grinding machine with diamond and alumina abrasive powders. Subsequently, polished samples were degreased using alcohol and were cleaned using an ultrasonic cleaning machine. The starting powders and the sintered samples were analyzed using an X-ray diffractometer (XRD; D8-Discover, Bruker AXS) with Cu-Kα radiation for phase identification. Spectra were registered between 20° and 80° with a step of 0.2° and velocity of 2°/min. Microstructures of sintered composite were observed using a laser optical microscope (VHX-5000; Keyence Co.) with 1000 × optical zoom magnification. Electron probe micro-analysis (EPMA, JXA-8200SP; JEOL Ltd.) was conducted with a scanning interval of 0.5 µm in the measurement range of 150 × 150 µm for structural characterization of

the surface morphology and for assessment of the component distributions of Si and Fe. The bending strength at room temperature was measured using a three-point bending test at room temperature with a span of 30 mm. The test sample of a bar of $3 \times 4 \times 40$ mm was prepared by cutting and polishing. Vickers hardness and fracture toughness were measured at room temperature at five or more points on the surface of sintered samples using a Vickers micro-hardness tester (FM-810e; Future-Tech Corp.) at loads of 0.98-4.98 N for 10 s. The indentation fracture method was adopted for measurement of the fracture toughness, as calculated using Eq. (1) [12,18].

$$K_{IC} = 0.016 \frac{P}{C^{1.5}} \left(\frac{E}{H_V} \right)^{0.5}$$

In that equation, K_{IC} represents the fracture toughness (MPa·m$^{0.5}$), H_V stands for the Vickers hardness (GPa), E denotes the elasticity modulus (GPa), P expresses the load (N), and C signifies the average half-length of the cracks formed around the corners of the indentations (m). The electrical resistivity was measured at room temperature using the four-terminal method of resistance measuring apparatus with test samples of a bar, which were the same as the samples used three-point bending tests.

3. Results and discussion

3.1. Characterization of the first-sintered body

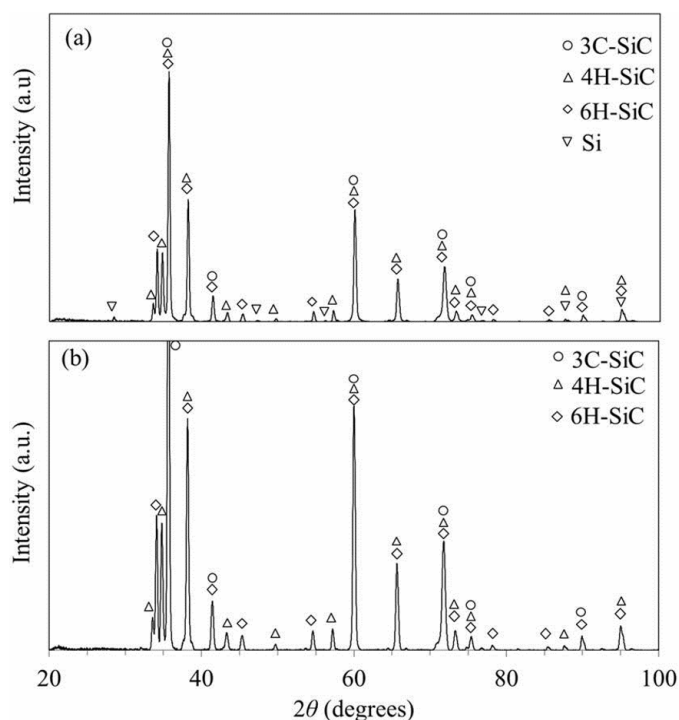The X-ray diffraction pattern of SiC powder before sintering is depicted in Fig. 3(a). In SiC powder, the diffraction peaks of SiC and Si were detected. However, the amount of Si was regarded as small. Three types of SiC were found: 3C, 4H, and 6H crystal structures. A strong diffraction peak of 3C-type was found. About 200 polytype structures of SiC have been reported to date: the most common SiC polytypes are 3C, 4H, 6H, and 15R [19]. These SiC polytypes of 3C, 4H, and 6H were regarded as formed through reaction during sintering in this study. However, only one polytype of Si was found. Its diffraction peak was identical to that of Si in Fig. 3(a). In addition, C was nanocrystalline. The resin was organic material.

The X-ray diffraction pattern of the first-sintered specimen is depicted in Fig. 3(b). Its diffraction peaks were similar to those depicted in Fig. 3(a), but no Si peak was detected. As depicted in Fig. 2, the disappearance of Si might result from the formation of SiC after reacting between Si and C in the formed body. Considering the compound ratio of raw materials, Si or C components of specimens would disappear during the first sintering. Here, polytypes of SiC were detected as 3C, 4H, and 6H.

3.2. Effects of infiltration metal on second sintering

X-ray diffraction patterns of second-sintered samples of SiC-1 and SiC-2 are shown respectively in Figs. 4(a) and 4(b). First, in the case of SiC-1, the diffraction peak was detected as almost identical to that shown in Fig. 3(a). Three types of SiC and Si were found. The peak intensity of Si was stronger than that of the SiC powder as a raw material. From the results, it was confirmed that the strong peak resulted from the molten Si which remained and infiltrated in the sintered specimen. Next, in the case of SiC-2, polytypes of SiC showed no differentiation by

Fig. 3. XRD patterns of (a) SiC powder and (b) the first-sintered body in SiC-1
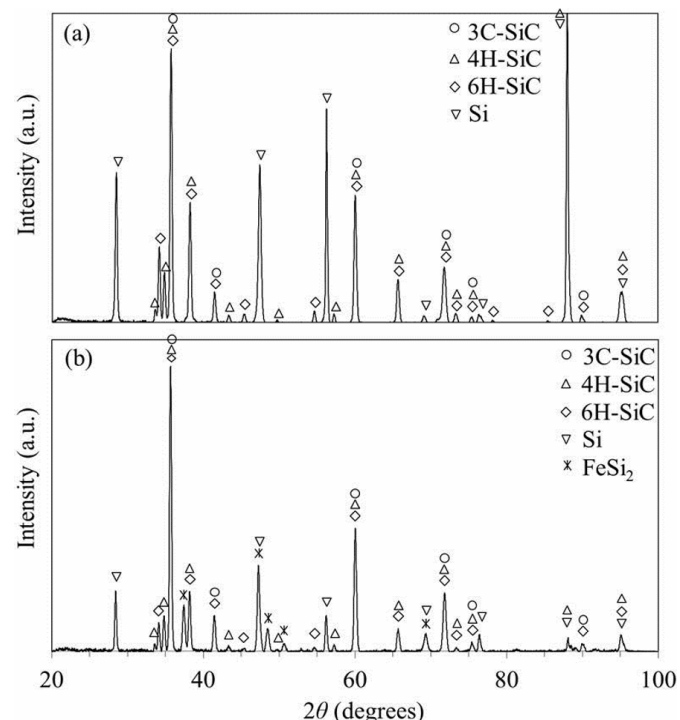

Fig. 4. XRD patterns of the second-sintered structure in (a) SiC-1 and (b) SiC-2

infiltrating of Si and Fe-75%Si alloy. In addition, a new peak of FeSi$_2$ appeared as depicted in Figure 4(b). As shown in the binary phase diagram [20], results demonstrate that the Fe-75%Si alloy structure consists of Si and FeSi$_2$ compound phase. The molten Fe-75%Si alloy remained in the sintered specimen without re-action and solidified during furnace cooling. Nevertheless, no reacted product of Fe was found. A new polytype of SiC had not formed. In fact, three types of 3C, 4H, and 6H-SiC had not changed by second-sintering even when using Fe-75%Si alloy. Results show that infiltration of molten Fe-75%Si alloy had lit-tle noticeable effect on the crystalline structure of sintered SiC.

Fig. 5(a) shows optical microscope images depicting the morphology of SiC powder of the raw material. The cross-sectional microstructures of second-sintered specimens of SiC-1 and SiC-2 are presented respectively as Figs. 5(b) and 5(c). The SiC powder consisted of particles with average particle diameter of 5 μm and of angular shape. No aggregated particle was found within the observation range, but each powder was confirmed clearly. By infiltration of Si, the microstructure of the sintered sample had become separated mainly to gray and white phases, as presented in Fig. 5(b). The microstructure of sintered sample by infiltration of Fe-75%Si alloy was almost identical to that of Si, but a part of the matrix structure was found to have different contrast as light gray phase, as presented in Fig. 5(c). From EPMA qualitative analysis and XRD analysis results, the SiC, Si and FeSi$_2$ components are represented respectively by gray, white, and light gray contrasts. Moreover, C or pores were observed in the back contrast. Because of infiltration of Si and Fe-75%Si alloy, both sintered structures were very dense, with low porosity. Considering the SiC particle shape before sintering as presented in Fig. 5(a), the sintering reaction was confirmed to have brought about the growth of SiC particles and boundary bonding. As a result, the SiC particles mutually joined to grow to 10 μm or more during reaction sintering. Other small grains were singly of 2 μm size but the SiC particles were clumped. Although many small joined particles were included in the sin-tered structure, they were closely enclosed by the molten Si and
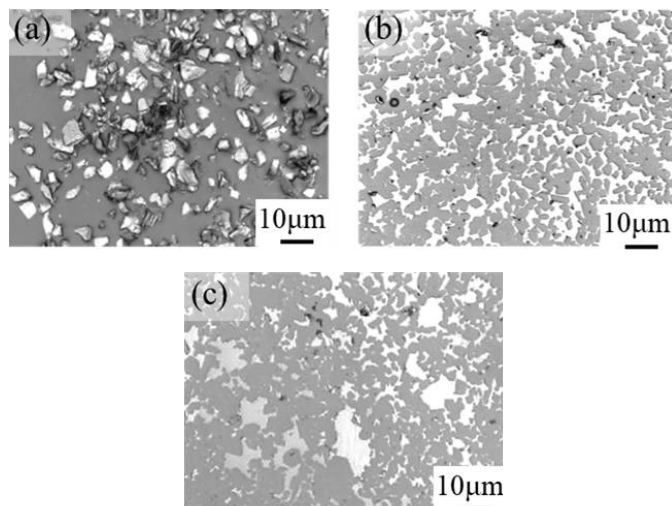
Fe-Si alloy. Regarding the SiC procedure, no differences were found between infiltration of molten Si and Fe-75%Si alloy, as presented in Fig. 5.

Next, an SE image and elemental distribution map of Si and Fe by EPMA in the second-sintered samples of SiC-1 and SiC-2 are depicted respectively in Fig. 6 and Fig. 7. The Si component was distributed overall in the observed structure because Si was included both in the matrix and in SiC particles. Although black parts of the structure resemble pores, C had not reacted with molten Si, as depicted in Fig. 6(b). Therefore, black parts were sketchy as the first-sintered body. The Fe compo-nent was not detected as depicted in Fig. 6(c). However, in the
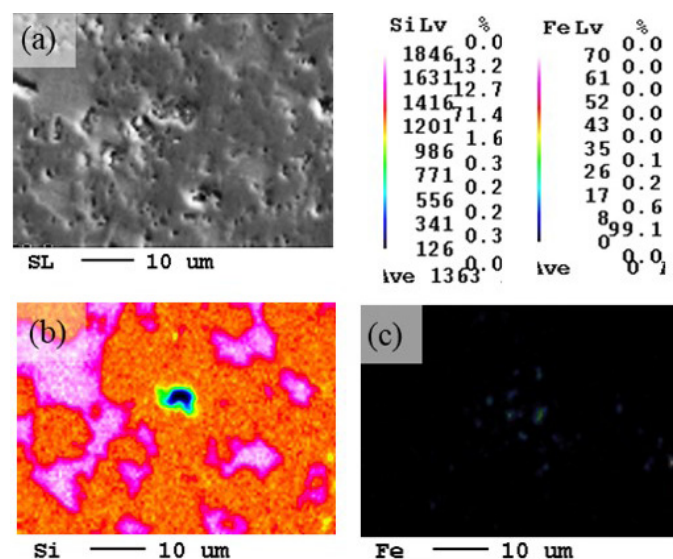

Fig. 6. (a) SE image and element mappings of (b) Si and (c) Fe of the second-sintered structure in SiC-1
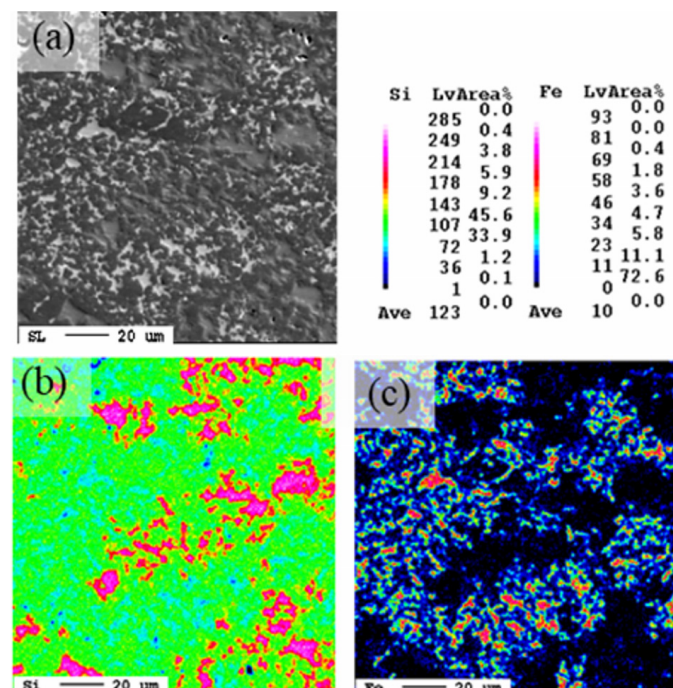

Fig. 7. (a) SE image and element mappings of (b) Si and (c) Fe of the second-sintered structure at SiC-2

Fig. 5. Microstructures showing (a) the appearance of SiC powder and cross-sectional second-sintered specimen in (b) SiC-1 and (c) SiC-2

case of SiC-2, white and gray phases were confirmed clearly. Two classes of compositions existed as the matrix, and were separated from one another. Results of element map analysis revealed that white phase contained Fe and Si, and that gray phase contained only Si, as shown in Fig. 7. The Si component was distributed throughout this observation range as shown in Fig. 7(b). The Fe component was detected as white phase only in the SE image of Fig. 7(a). From XRD analysis results, we found that Fe existed as $FeSi_2$ phase; the high-Si concentrated part is merely the Si phase.

Fig. 8 presents a magnified view of Fig. 7(a), with SiC shown as the gray phase, Si as the light gray phase, and FeSi2 as the white phase. Results demonstrated that $FeSi_2$ and Si phase were separated completely in the matrix. Additionally, $FeSi_2$ phase was not crystallized into the Si phase, and vice versa. Irrespective of the SiC particle size, the grains were enclosed closely by the Si and $FeSi_2$ phase. Even if the structure was such a feature in Fig. 8, the porosity was extremely low. Results confirmed that the infiltrated Fe-Si alloy had sufficiently excellent performance of infiltration into the preformed body. A newly formed and grown SiC is obtainable by reaction between the Si component of molten Fe-75%Si alloy and C component of the preformed specimen. Furthermore, the SiC would be deposited to form in the molten alloy because the sublimation point of SiC is 2818 K or higher. Therefore, SiC formation occurred before the solidification of molten Fe-Si alloy. No difference was found between Si and $FeSi_2$ phases for SiC formation, as shown in Fig. 8. Moreover, the gap of the body can be filled by molten Si because of Si expansion by about 10 vol.% when solidified.
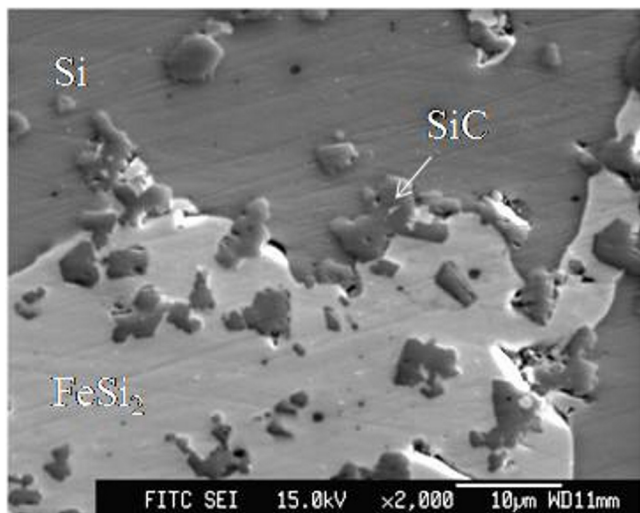

Fig. 8. SEM image showing a magnified view of Fig. 7

3.3. Effects of compound composition of samples on second sintering

Surface appearances of the second-sintered specimen are shown in Fig. 9. The sintered specimen of SiC-2 exhibited metallic luster, as shown in Fig. 9(a). In the case of SiC-3, the surface appearance presented no metallic luster, as shown in

Fig. 9(b). Additionally, cracks and distortions were generated in both sample plates. The main compound of SiC-2 sample was SiC of 73%, whereas that of SiC-3 sample comprised Si of 42% and C of 42%. Here, SiC powder used as a raw material had not changed during sintering because it was not reacted by infiltrating Si and Fe-Si alloy, i.e., the SiC powder acted as an aggregate having high stiffness. However, Si and C powder easily reacted during both first sintering and second sintering. Contraction or expansion of the specimen body occurred by reaction with SiC formation in a coordinated presence of Si and C. For that reason, the dimensional change became large. In the condition of SiC-3, Si and C were contained respectively by 26.4 at.% and 73.6 at.%. The C content was about three times higher than Si. Actually, SiC is a covalent bond between Si and C with the atomic ratio of Si : C = 1:1. In addition, the Si component disappeared. The C component decreased by the first reaction sintering. Furthermore, the remaining C reacted with the Si component of molten alloy. Consequently, the body expanded by SiC formation on reaction. That expansion ratio was about 1.9 times before and after reaction of C to SiC. Results suggest that the body crack caused the expansion by SiC formation.
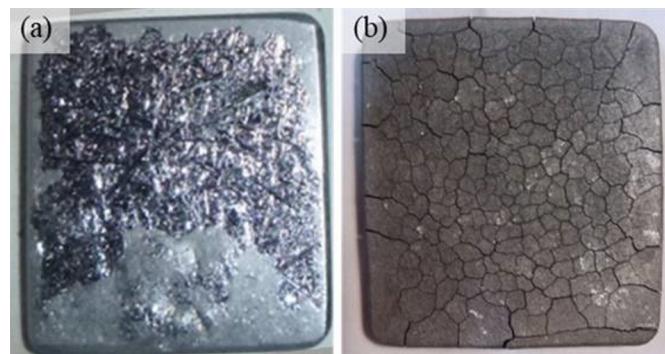

Fig. 9. Appearance of the second-sintered SiC of (a) SiC-2 and (b) SiC-3

X-ray diffraction patterns of the second-sintered sample SiC-3 are presented in Fig. 10, where 3C-SiC, Si, and $FeSi_2$ were detected. The polytype of SiC was identified only as 3C-SiC. Based on these results, 3C-SiC was confirmed to have been formed by second reaction sintering. The sintered SiC, as shown in Figs. 4(a) and 4(b), consisted of three polytypes: 3C, 4H, and 6H-SiC. Only 3C-SiC formed by growth through infiltration of molten Si and Fe-75%Si alloy. Actually, 3C-SiC form more easily at temperatures lower than 1873 K than reported results for the formation of SiC of other types [1,19]. For other sintering methods such as hot pressing, HIP, treatment at temperatures of 2273 K or higher was necessary for sintering SiC. The reaction sintering method used for this study is an easier process than that of other methods because the sintering of SiC can be done at a lower temperature. Although the C contents of SiC-3 were much higher than those of SiC-2 in the first-sintered specimen, the Fe component was detected as only $FeSi_2$ phase in SiC-1 as well as SiC-2. Therefore, results demonstrated that the Fe component did not form carbide but instead formed $FeSi_2$ when sintered using Fe-75%Si alloy.
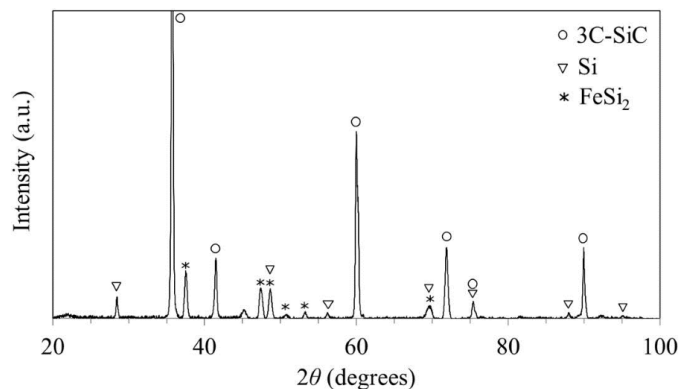
Fig. 10. XRD pattern of the second-sintered structure in SiC-3

An SE image is presented in Fig. 11 along with an EPMA elemental distribution map of Si and Fe in the second-sintered samples of SiC-3. The joined black phases appeared as SiC throughout the observed structure. The area representing SiC in SiC-3 was occupied more widely than that of SiC-2. Moreover, SiC was not shaped as unique grains, but with all grains being joined. The matrix area was small. Furthermore, the SiC gap was filled by Si and $FeSi_2$ phases. The $FeSi_2$ phase was identified by its wider white parts compared to other parts of the Fe distribution, as presented in Fig. 11(c). It was about 20 µm and narrowly shaped. Spots having high concentration of Si appeared sparsely in the structure. The amount of SiC formation of sample SiC-3 was larger than that of sample SiC-2 because the C contents of SiC-3 were higher as well. Therefore, the Si component of the molten Fe-Si alloy increased during second-sintering. For the reason presented above, the highly concentrated Si part was smaller than the part, as shown in Fig. 7(b). Although several spots were found with highly concentrated Fe in the structure, XRD results presented in Fig. 10 demonstrate that only $FeSi_2$
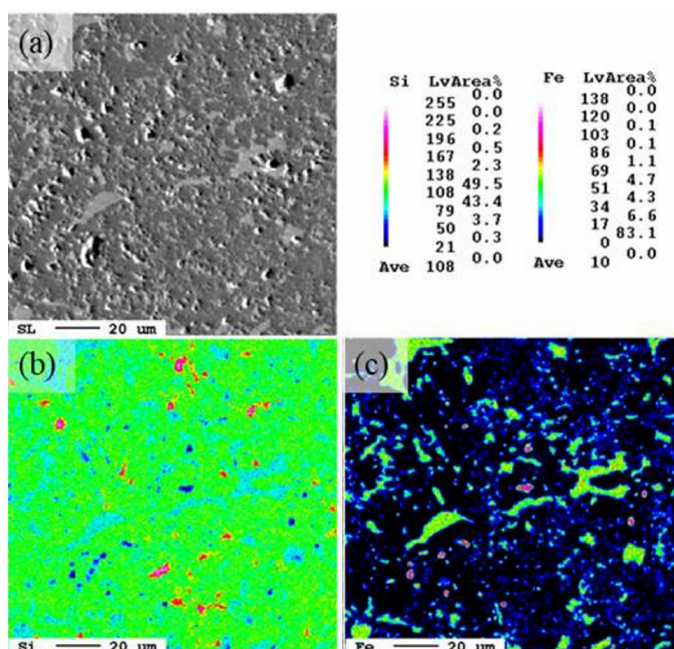
had been detected as only FeSi phase. These microstructure observation results clarified that the sintered structure consisted of SiC, Si, and $FeSi_2$. Sintered SiC composites with more desirable performance could be produced as new materials if the raw materials and the composition of sintering alloys could be controlled for each process.

Fig. 12 presents a magnified view of Fig. 11(a). The crystallized SiC grains were mutually joined, with very small pores in SiC parts. These findings suggest that the pores were generated in unsintered parts with because the C powder as an ultra-fine raw material that was easily agglomerated. When the C powder aggregates are presented, the molten alloy can not infiltrate into the aggregate. Figure 13 presents a schematic illustration of the relation between porosity and infiltration. In a low-porosity body, SiC might form by contacting the molten alloy on the body surface. Then, the pore or gap would almost close on the surface by volume expansion because of SiC formation. The molten alloy could not be more deeply infiltrated than there. For this reason, if a preformed body with high density and high C content were prepared, then the molten alloy would not be deeply infiltrated into the body. Reportedly, the SiC layer thickness obtained by Si and C reaction at 1703 K for 10.8 ks was about 10 µm [21]. Based on that finding, we inferred that the molten alloy can be infiltrated by diffusion through the SiC layer from the surface over a long period of time. Therefore, the balance between the porosity by first sintering and volume

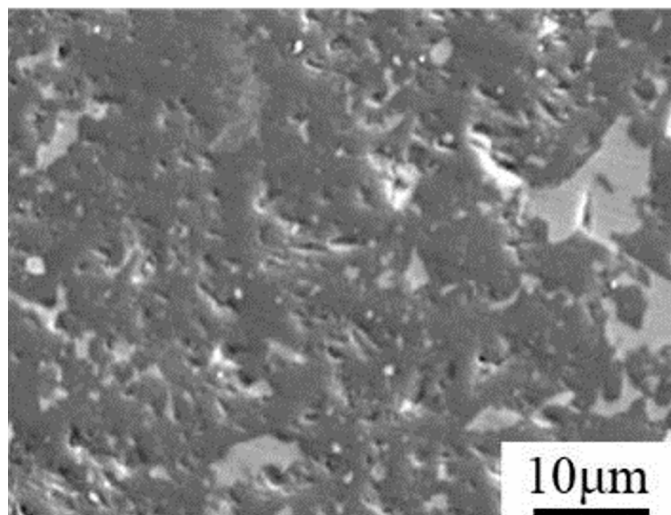Fig. 12. SEM image showing a magnified view of Fig. 11(a)

Fig. 11. (a) SEM image and element mappings of (b) Si and (c) Fe of the second-sintered structure in SiC-3
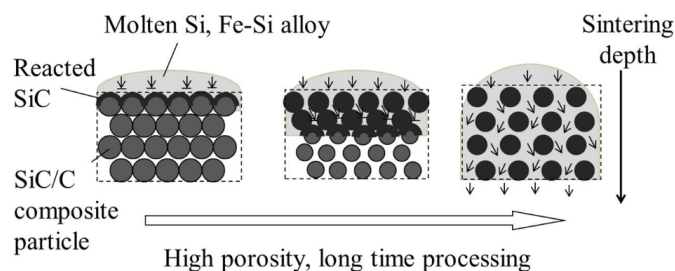

Fig. 13. Schematic illustration of relation between porosity and infiltration

expansion must be controlled by second sintering to fabricate a composite that has low porosity, no cracking, and sufficient SiC content.

3.4. Mechanical properties of sintered SiC composite materials with Fe-Si alloy

Table 2 presents properties of the sintered SiC in SiC-1 and SiC-2. Sample SiC-3 measurements were excluded because many cracks and distortions were generated at the surface and inner specimen and because sample pieces could not be manufactured for measuring tests. Density measurements were done using Archimedes' method: JIS R 1634. The SiC-1 and SiC-2 densities were, respectively, 2.75×10^3 kg/m^3 and 3.25×10^3 kg/m^3. As described earlier, the sintered SiC in SiC-2 included a larger component of Fe than that of SiC-1 did. Furthermore, the density of general SiC ceramics using a hot-pressing method was found to be 3.21×10^3 kg/m^3. The density of sintered SiC in this study was almost equal to that obtained using the hot-pressing method. Furthermore, their respective open porosities were 4.8 vol.% and 1.2 vol.%. The sintered SiC with Fe-75%Si alloy became very dense. Both of these hardness values were measured using Vickers hardness testing as about 2.0 GPa. Little difference was found between SiC-1 and SiC-2. The SiC hardness found in this study was similar in quality to that found for SiC ceramics from other studies [9,12]. Most of the sintered structure is occupied by the area of the SiC. Therefore, the hardness was unchanged, being independent of the state of the matrix. For the bending strength, no difference was found between SiC-1 and SiC-2 either because the samples infiltrated by Si and Fe-Si alloy have hard and brittle phases. The fracture toughnesses of SiC-1 and SiC-2 were, respectively, 3.1 MPa·m$^{0.5}$ and 4.0 MPa·m$^{0.5}$. The fracture toughness of SiC ceramics produced using other methods had been reported as 2.0–4.5 MPa·m$^{0.5}$ [1,9,12,15]. The matrix of sintered SiC is expected to be brittle in the same way, obeying the bending rule of strength, but the fracture toughness was improved about 30%. Regarding results of observations of tested samples after indenting, the matrix boundary of FeSi$_2$ is presumed to be effective for suppression of crack propagation. Moreover, it was important to lower the Si component for matrix toughness improvement. Although several phases would appear by changing Si concentration from the Fe-Si binary phase diagram [20] and although that phenomenon during sintering would be complicated, it was inferred that the fracture toughness can be improved by increasing the Fe component for Si consumption by formation of SiC. Therefore, it would be effective to have the structure

presented in Fig. 11 and 12. Finally, the electrical resistivity of sample SiC-2 was much lower, in fact close to two orders of magnitude lower, than that of sample SiC-1. The electrical resistivity of FeSi$_2$ phase was found to be 1×10^{-5}-5×10^{-3} Ωm. The electrical resistivity of FeSi$_2$ phase was much lower than that of Si [14,22,23]. The resistivity of general SiC produced using a hot-pressing or single-crystal is not low. The value is 1×10^4-10^{10} Ωm [24]. Therefore, improvement of the electrical resistivity of sintered SiC materials can be achieved by FeSi$_2$ phase using Fe-75%Si alloy, thereby realizing high performance of SiC. As a result, electrical discharge machining (EDM) can be applied for sintered SiC. These are mainly machining methods of two kinds: die-shrinking using a Cu or graphite electrode, or wire-cutting using an electrode line of Cu-Zn alloy. The SiC ceramics produced, even in complicated shapes, using this process can be machined with high precision as easily as steel using commercially available machines. Results demonstrated that the machinability of sintered SiC ceramics can be improved using the fabrication methods used for this study.

Since last year, a steel manufacturer in Japan has been testing SiC ceramic rollers, specifically a guiding roller for a rolled bar. The product is a guiding roller for a rolled bar. This roller is used for controlling the direction of passage of the bar. Furthermore, the direction is the groove of a finishing mill roll. The inner diameter allowance of the product was ±0.025 mm. Its surface roughness (Ra) was <1.6 µm. All the product requirements were fulfilled using EDM of die-shrinking and wire-cutting for sintered SiC. The testing evaluation results have been good. It can not be controlled merely by changing the SiC formation if the improved performance of the electrical resistivity and the fracture toughness were conducted. The results obtained from this study confirmed that selecting high-performance materials for use as the SiC composite improved the SiC ceramic properties. The molten Fe-75%Si alloy and the reaction sintering of SiC were very compatible. Improving the performance of weak points and improving infiltration into the preformed body were identified as important. The molten Fe-Si alloy can infiltrate deeply into the preformed body. Moreover, Si and FeSi$_2$ phases were separated and finely distributed into the sintered structure matrix. Results show that high-precision machining was conducted using EDM. However, several iron silicide phases would appear if the Si concentration in the structure were changed considerably during reaction sintering. The sintered structure would come to contain many phases and would be complicated by phase formation and separation, and by SiC formation. To characterize and avoid those complications, future studies must investigate their mutual relations.

TABLE 2

Properties of sintered SiC with Si and Fe-Si alloy

Sample	Density (10^3 kg/m^3)	Open porosity (Vol.%)	Vickers hardness (GPa)	Bending strength (MPa)	Fracture toughness (MPa·m$^{0.5}$)	Electrical resistivity (Ωm)
SiC-1	2.75	4.8	1.9	299	3.0	1×10^{-1}
SiC-2	3.25	1.2	2.0	290	4.1	9×10^{-3}

1652

4. Conclusions

The Fe-Si alloy exhibited excellent performance of infiltration into the first-sintered body. For sintering, it was able to react for sintering similarly to Si metal such that the structure of sintered SiC with Fe-Si alloy had very low porosity. The SiC formation was affected only slightly by changing from Si to Fe-Si alloy. It is useful in the same way as composite materials of SiC / Si / FeSi$_2$. This study demonstrated the considerably decreased electrical resistivity of SiC by reaction sintering with Fe-Si alloy without decreasing its mechanical performance compared to that of Si. Results also confirmed that high-precision machining can be applied to sintered SiC ceramics. Therefore, it is expected that many difficulties experienced with SiC ceramics can be alleviated and can be eventually resolved by controlling the sintered structure using various infiltrating metals and blending of raw materials.

REFERENCES

[1]   H. Tanaka, J. Ceram. Soc. Japan **110** (10), 877-883 (2002).

[2]   M. Iwasa, M. Kinoshita, J. Ceram. Soc. Japan **108** (2), 206-209 (2000).

[3]   S. Hiratsuka, J. Japan Foundry Soc. **82**, 769-771 (2010).

[4]   K. Nakano, A. Kamiya, H. Ogawa, Y. Nishino, J. Ceram. Soc. Japan **100** (4), 472-475 (1992).

[5]   M. Suzuki, Y. Inoue, M. Sato, T. Ishikawa, K. Goda, J. Mat. Sci. Japan **52** (6), 681-687 (2003).

[6]   K. Asano, H. Yoneda, J. Japan Foundry Soc. **81**, 529-535 (2009).

[7]   H. Gu, H. Nakae, J. Japan Foundry Soc. **76**, 909-914 (2004).

[8]   J.N. Ness, T.F. Page, J. Mater. Sci. **21**, 1377-1397 (2010).

[9]   S. Suyama, T. Kameda, Y. Itoh, Diam. Relat. Mater. **12**, 1201-1204 (2003).

[0]   H. Nakae, H. Yamaura, Y. Sugiyama, J. Japan Foundry Soc. **75**, 29-34 (2003).

[11]   H. Kaneda, T. Choh, J. Japan. Inst. Light Met. **45** (10), 537-542 (1995).

[12]   A.J. Whitehead, T.F. Page, J. Mater. Sci. **27**, 839-852 (1992).

[13]   Y. Fukuzawa, N. Mohri, Int. J. Japan Soc. Prec. Eng. **64** (12), 1731-1734 (1998).

[14]   Ch. Kloc, E. Arushanow, M. Wendl, H. Hohl, U. Malang, E. Bucher, J. Alloys Compd. **219**, 93-96 (1995).

[15]   V. Milekhine, M.I. Onsoien, J.K. Solberg, T. Skaland, Intermetallics **10**, 743-750 (2002).

[16]   A. Ciftja, T.A. Engh, M. Tangstad, Metall. Mater. Trans. A **41**A, 3183-3195 (2010).

[17]   G.W. Liu, M.L. Muolo, F. Valenza, A. Passerone, Ceram. Int. **36**, 1177-1188 (2010).

[18]   F. Sergejev, M. Antonov, Proc. Estonian Acad. Sci. Eng. **12** (4), 388-398 (2006).

[19]   L.K. Fevel, D.R. Petersen, C.K. Saha, J. Mater. Sci. **27**, 1913-1925 (1992).

[20]   T.B. Massalski, Binary alloy phase diagrams, II Ed. ASM International 1772 (1990).

[21]   H. Zhou, R.N. Singh, J. Am. Ceram. Soc. **78** (9), 2456-2462 (1995).

[22]   M.Ito, H. Nagai, E. Oda, S. Katsuyama, K. Majima, J. Mater. Sci. **37**, 2609-2614 (2002).

[23]   https://en.wikipedia.org/wiki/Electrical_resistivity_and_conductivity, accessed: 18. 09.2018.

[24]   Y. Takeda, K. Nakamura, K. Maeda, Y. Matsushita, J. Ceram. Soc. Jpn **95**, 860-863 (1987) .